This is a repository copy of *Diode area melting of Ti6Al4V using 808 nm laser sources and variable multi-beam profiles*.

White Rose Research Online URL for this paper:
https://eprints.whiterose.ac.uk/184669/

Version: Published Version

Article:

Diode area melting of Ti6Al4V using 808 nm laser sources and variable multi-beam profiles

Mohammed Alsaddah [a,*], Ashfaq Khan [a], Kristian Groom [b], Kamran Mumtaz [a]

[a] Department of Mechanical Engineering, University of Sheffield, Sheffield S1 3JD, UK
[b] Department of Electronic & Electrical Engineering, University of Sheffield, Sheffield S1 3JD, UK

HIGHLIGHTS

- Multi-laser approach with potential to overcome traditional laser powder bed fusion processing challenges (e.g scalability, processing efficiency and thermal control).
- Multi-beam profiles influence microstructure (grain size) and mechanical properties of diode area melted components.
- Low laser wavelength efficient energy absorption assisted generation of powder bed temperatures exceeding 2000 °C.
- Generation of reduced melt pool cooling rate compared to traditional laser powder bed fusion (600 °C/s compared to 10^5-10^7 °C/s).
- Process was able to promote the development of a β phase within the manufactured Ti6Al4V component.

GRAPHICAL ABSTRACT
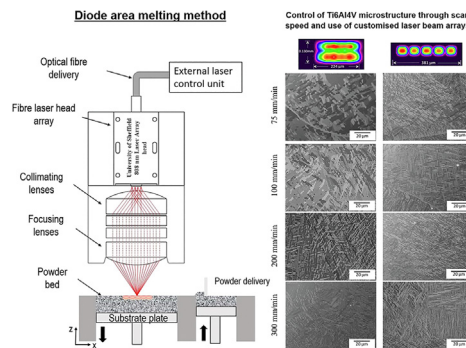
ARTICLE INFO

ABSTRACT

This paper presents an alternative to traditional laser powder bed fusion (LPBF), using an efficient, highly scalable multi-laser additive manufacturing methodology known as Diode Area Melting (DAM). DAM integrates multiple individually addressable low power fibre coupled diode lasers into a laser head, these traverse across a powder bed to melt powdered feedstock. The highly scalable and compact diode lasers operate at a shorter wavelength and lower powers compared to traditional LPBF fibre lasers, enabling a more efficient energy absorption, with an increase of up to 14%. In this study, a bespoke multi-laser head was used to process Ti6Al4V powder using ten 5 W 808 nm diode lasers simultaneously. Multi-layer parts were produced with a maximum density of 98% with variable beam profiles shown to greatly influence melt pool formation, microstructure and mechanical performance (4–5 GPa hardness and elastic moduli up to 120 GPa). DAM was able to generate lower cooling rates than traditional LPBF systems (600 °C/s compared to 10^7 °C/s), with variable beam profiles altering grain size and promoting the development of a β phase within components.

* Corresponding author.
E-mail addresses: mtalsaddah1@sheffield.ac.uk, alsaddah@gmail.com (M. Alsaddah).

1. Introduction

Laser Powder Bed Fusion (LPBF) Additive Manufacturing (AM) technologies such as Selective Laser Melting (SLM) and Direct Metal Laser Sintering (DMLS) are now viewed as disruptive, viable alternatives to traditional manufacturing approaches. LPBF is increasingly used to manufacture within aerospace, automotive and energy sectors to manufacture high-value end-use components (e.g GE fuel nozzles for the LEAP engine, Airbus A380 spoiler hydraulic manifold). LPBF's increased usage and industrial uptake is due to the capability of the process to create customised, geometrically efficient structures with low material wastage from a variety of metallic alloys that would otherwise be difficult or impossible to produce using conventional manufacturing techniques. LPBF processes such as SLM use high power fibre lasers (typically 200–1000 W) to generate a focused high energy density laser spot ($\sim$40–100 μm diameter) to melt regions of a thin layer of pre-deposited metallic powder feedstock layer upon layer. These lasers are deflected across the powder bed using a mechanically directed galvanometer (galvo) mirror to selectively melt cross-sections of a powder bed based upon sliced 3D CAD data [1,2]. A similar non-laser based powder bed fusion approach known as Electron Beam Melting (EBM) instead uses an electron gun (3–6.5 kW) in a vacuum, deflected using a magnetic field to scan and melt the powder bed. Compared to LBPF, EBM systems generate less thermal residual stress within the process (due to the ability to pre-heat the surface with the electron beam) and have a higher build rate (due to faster electron beam scanning and ability to split/control multiple electron beams on the powder bed). EBM hardware is generally more expensive than those used in LPBF, and creates components with poorer resolution and surface finish. Because of this, LPBF are currently the most widely used AM systems in industry for the creation of fully functional complex metallic components.

1.1. State-of-the-art LPBF manufacturing challenges

The methodology for manufacturing components using LPBF has not fundamentally evolved in over two decades. The use of high power fibre laser sources, creating high intensity laser spots that rapidly deflect across the powder bed using galvo-mirrors creates a number of challenges for LPBF [3]. These challenges include limitations for processing efficiency, scalability, thermal/microstructural control and range of processable alloys.

1.1.1. Laser processing efficiency and absorption

Lasers used in LPBF systems are selected primarily for their high power and beam quality regardless of the absorption spectrum of the material being processed. Presently used laser systems employ fibre lasers operating at wavelengths of $\sim$ 1070 nm. At 1070 nm, depending on the material being processed, only a portion of the laser energy is absorbed/converted to heat, this contributes further to the energy loss as a consequence of the high reflectivity in metals at this wavelength [4]. Current LPBF lasers are already inefficient with typically 20–30% wall-plug efficiency, requiring higher powers to process the more reflective materials such as copper, aluminium etc. Alsaddah *et al.* showed that the absorptivity of Ti6Al4V increases by 14% when using a single 808 nm laser compared with 1064 nm, and by 25% at 450 nm [5]. For highly reflective metals such as copper, the absorptivity increases from $\sim$ 5% for 1064 nm to 86% for a 450 nm laser source.

1.1.2. Single fibre laser productivity

The galvo-scanning method for deflection of fibre laser sources over a limited working area has inherent implications for system productivity and scalability. Low productivity has been identified as one of the limiting factors to wider spread adoption of SLM by industry, especially when manufacturing higher volumes or when serial production is required [6]. The build rate of LPBF is between 2 and 40 cm³/h for a single laser, depending on the material being processed [7]. Literature to suggests that optimization of processing parameters for a single laser source generates limited practical productivity increases for LPBF [12].

1.1.3. Rapid solidification

Because the LPBF approach uses fast-moving (up to 7000 mm/s), highly focused melting sources the process generally exhibits poor thermal control over the melt pool with high cooling rates (up to 10^7 °C/s) generating microstructures that are fine dendritic and difficult to alter in-situ. The rapid cooling rate also creates large thermal residual stresses within the manufactured part that need to be relieved post-process [13]. Occasionally, the stress can be so large that it causes a part to crack or geometrically distort/fail within a build. Rapid solidification can limit material processability, making it challenging to process high performance, intermetallic forming alloys that exhibit limited weldability, leading to a high crack susceptibility (e.g high gamma prime alloys such as CM247LC, TiAl, Al6000 series etc.) [14-16].

1.2. Development of multi-laser fibre systems

To overcome LPBF productivity limitations, system manufacturers (e.g Renishaw, EOS, SLM Solutions) have developed systems that include up to four high power (500–1000 W) fibre lasers (with one system up to twelve lasers, SLM Solutions NXG XII 600), leading to increased build speeds but also significant increases in hardware costs, energy consumption and overall system size [6,7,17-19]. The use of multiple galvo-scanning systems has future potential to enhance in-situ thermal control. However, this control enhancement is likely to be small, with only marginally altered cooling rates due to the continued use of highly focused, rapidly scanning laser beams. It has been reported the build rate for Ti6Al4V of a four laser SLM system is 105 cm³/h compared with 18 cm³/h for a single laser system. A cost model developed by Kopf *et al.* showed that implementing twenty-seven lasers of 1 kW power each would increase the build platform from 1400 cm² to 3540 cm², Therefore, reducing the production cost by 43% compared to a system with two lasers of 700 W [20]. However, the authors state that implementation of such a large number of lasers is not technically feasible. In the course of integrating multiple fibre lasers there are practical space considerations, as each laser requires an individual galvo-scanning mirror, cooling system, optics and control. Essentially the cost of an SLM system scales super-linearly with the number of lasers, whilst the scanning speed of each laser is still restricted by the mechanical movement of the galvo-mirror system. Furthermore, the processing area is limited by the ability of the F-theta lens to provide a consistent beam profile and laser power across the processing area. Lasers consume approximately 68% of the electrical energy in SLM systems due to the low conversion efficiency of electrical to optical energy, which is of the order of 10–30% [21].

1.3. Alternative approaches to traditional LPBF

High Power Diode Lasers (HPDL) are being explored as alternative laser sources for use within LPBF, they are more compact and energy-efficient than fibre lasers and have longer lifetimes [22]. The ability of HPDL to emit short wavelengths (450 nm-3300 nm) with up to 60% wall-plug efficiency has promoted their use within material processing applications such as soldering, cutting, surface treatments, and welding [22]. Matthews et al. used addressable single diode lasers as heat sources in an attempt to

increase LPBF productivity. The researchers applied a diode-based additive manufacturing (DiAM) method to four 1.25 kW stacked diode arrays (comprising of 60 individual laser bars) to provide a total of 5 kW optical power at a wavelength of 1007 nm [23]. The incoherent output beam was homogenized by a liquid crystal light valve along with a Q-switched Nd: YAG Laser Beam as a hybrid laser with a wavelength of 1064 nm. This was used to melt an area of 2–3 mm for each layer in a single exposure. However, the complexity of the optical system and the short laser pulse through the photomask restricted the processing field to 2×2 mm^2. Furthermore, the long wavelength of the lasers used in DiAM and the available output power of 20 J/cm^2 incident on the powder bed limited the process to low melting temperature metals (Sn powder). Studies of part density and processing efficiency have not yet been reported. Another multi-spot LPBF system has been developed by Fraunhofer ILT that does not require galvo-mirrors to direct the irradiated laser energy onto a powder bed. Instead, it uses a fixed array of multiple laser spots moving on a gantry system [24]. These multiple high power laser spots create a controllable intensity distribution to create 3D structures with high flexibility in terms of productivity and building space. However, to generate high-power multi-laser spots with a wavelength of 976 nm capable to melt the powdered feedstock, several laser diode modules need to be incorporated to form a single spot of 200 W [25]. A multi-diode laser approach named Diode Area Melting (DAM) was introduced by investigators at The University of Sheffield [26], designed to use low laser powers with more efficient absorption profiles for LPBF. An 808 nm single diode module comprising 19 emitters was focused using cylindrical micro-lenses and used to cover a processing area 4. 75 mm $\times$ 0.25 mm as a linear stripe. Each emitter contributed an output power of 2.5 W, which in total supplied 50 W (power density of 4.21×103 W/cm^2) and a 99% dense component of 316L stainless steel powder was fabricated. This work was able to initially prove that utilisation of wavelength optimised lasers could efficiently melt powders with temperatures exceeding 1300C using less than 2.6 W laser power per emitter and reduction in overall component residual stress [5,26-28]. Alsaddah et al. explored the use of shorter 450 nm lasers as a potential candidate laser sources for the DAM process [5]. It was found that use of shorter wavelength lasers improved processing efficiency/absorption when using low power 4.5 W lasers to process Ti6Al4V powders.

In this paper, we investigate the use of up to ten low power diode lasers (less than5 W each) in a configuration that is potentially scalable to large write areas without speed/resolution/deformation penalty. A short laser wavelength of 808 nm is used so that high absorption and high processing efficiency can be achieved. Furthermore, individual control of each laser allows the management of intensity distributions across the linear array of laser beams, enabling complex custom parts to be built. The aim of the work is to realise a high resolution and high energy-efficiency AM system, with improved process thermal control, which has the potential to be scalable to write areas of appropriate dimension for production.

2. Diode area melting laser head system design and activated beam profiles

The optical system used in this work is illustrated in Fig. 1(a). Multiple individually addressable laser sources traverse the powder bed in a parallel. This system has evolved from previous DAM work previously reported [26-28] and now uses fibre-coupled diode sources coupled into a bespoke laser head rather than using a single diode emitter bar. Short-wavelength (808 nm) 5 W fibre lasers are used, the short wavelength ensures strong absorptivity whilst the fibre delivery ensures good beam

quality and allows the laser diodes to be located away from the processing environment. As indicated in Fig. 1(b), the fibre-coupled laser diode modules are connected to a customized 2-D fibre array head (2D-FAH). The 2D-FAH consists of a 2D array of v-groove lines. Each linear array has 50 multimode fibre channels with a 105 μm core and a numerical aperture of 0.22NA. The overlap of adjacent melt pools is essential for high part density. As such, the fibres were positioned at 127 μm centre-to-centre spacing, giving a total width of 6.35 mm. An imagining lens was used to relay emitted light from the v-groove array and focus onto the powder bed. The relay optics collimate and focus each beam from the 2D FAH at a magnification of $\times$ 0.6. Therefore, each beam is focused to an individual Gaussian profile with a spot size of 65 μm to give a total width of 3.5 mm at a focal length of 63.5 mm. The laser head assembly was designed to allow for in-situ pre/post-heating or re-melting during the process. A post-heating scanning strategy was used to homogenize the temperature field and reduce the cooling rate by using the second linear array as heat input after the first array (melting lasers) passed by.

Though the developed laser head has the potential to use up to hundred laser sources simultaneously during DAM processing only ten lasers will be utilised for this study in order to better understand on a small scale multi-laser interaction and effect on melt pool formation. In this study, three laser beam profiles were activated within the laser head: laser profile-1 (LP1), profile-2 (LP2) and profile-3 (LP3), as shown in Fig. 2. LP1 uses ten lasers within two arrays, this should enable either a pre/post-heating effect or re-melt of the melt pool during scanning and perhaps reducing the melt pool cooling rate. LP2 uses a single line array of ten lasers, this should increase write width compared to LP1 but increase cooling rate. LP3 uses a single line array with a gap between each laser (254 μm centre-to-centre pitch between the fibres) will likely create the largest write-width when using ten lasers. A constant current laser driver was used to control each laser source and vary power as the laser assembly traverses the powder bed to create the component using a two-axis gantry system. A vertical translation stage is also included in the system to allow for focusing adjustments. The output of each single laser power is defined by a PC control system.

3. Experimental methodology

Ti6Al4V alloy powder (Carpenter Additive, UK) with a particle size of 15–50 μm was used during DAM processing. The material composition of the Ti6Al4V powder is Ti (balance), Al (~5.8 wt%), V (~3.8 wt%), Fe (~0.3 wt%), O (~0.15 wt%), C (~0.02 wt%), N (~0.05 wt%), H (~0.03 wt%). A custom-built chamber was purged with argon to avoid oxidation during processing. An argon air knife with filtered gas re-circulation passes over the processing area to reduce spatter from reaching the laser head and settling onto the powder bed. The laser head traverses over the powder bed in the x-y axis with speeds ranging between 10 mm/min up to 1000 mm/min. An IR-Pyrometer (CTLM-2H, Micro-Epsilon UK Ltd) has been incorporated into the system at an angle of 60^0 to measure the surface temperature during the process. The investigation was conducted in multiple stages. Initially, two lasers were activated at variable pitch/distances to establish the optimum profile configuration required to produce fully fused continuous solid tracks and melt pool characteristics. This enabled the selection of a suitable laser beam profile arrangement to be used for single-layer parts. After this, five lasers were activated using the optimal beam profile configuration previously developed to process single layers on 1 mm thick powder. An analysis of the melt pool was conducted to understand and develop control over laser processed sample density and surface roughness. The next stage was to develop an
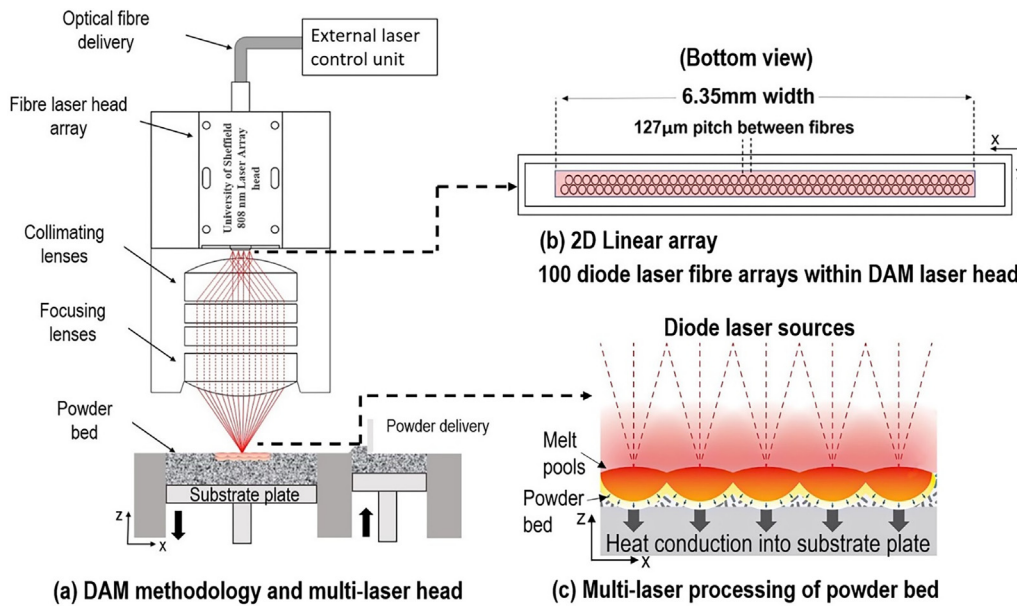
Fig. 1. (a) Schematic of DAM (b) laser head beam profile configuration (c) schematic of melt pool.
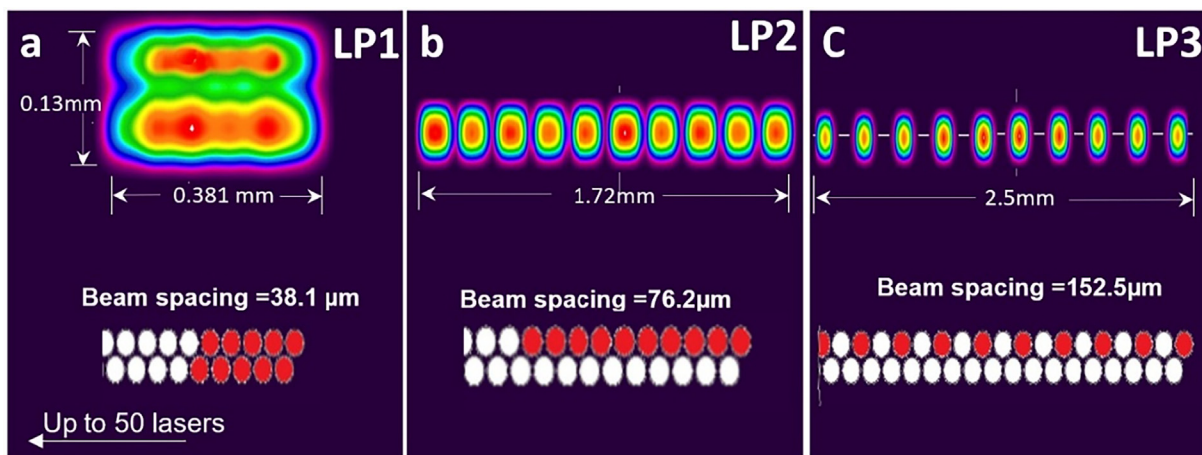
Fig. 2. Measured beam profiles for activated laser fibres within DAM laser head (a) LP1 (b) LP2 (c) LP3.

energy normalization model, following the work undertaken by Thomas *et al.* [29], to determine the process parameters for multi-layer parts using ten simultaneous laser sources. In the final stage of this work, the microstructure and mechanical properties of manufactured parts are analysed and compared with components produced using a commercial LPBF systems. As proposed by Spierings *et al.* [30], the Archimedes principle was used to measure the density. Samples showing densities > 95% were selected and then used to measure the surface roughness. These were then hot mounted and polished to be examined for microstructure and mechanical properties. X-Ray diffraction (D2 Phaser -Bruker) was used to conduct phase and microstructure analysis (XRD) within the range of $2\theta = 20^o - 100^o$ with steps of 0.02^o. The nano-hardness was conducted with a 4×4 matrix using an open-loop trapezoidal method of loading and unloading, with a 5-sec hold per stage at 13,000 µN maximum loads using a Triboindenter. The average surface roughness was measured using an optical 3D microscope (Alicona infinite focus). Microstructural analyses was conducted using a scanning electron microscope SEM (Tescan VEGA3) equipped with an electron back-scattered diffraction (EBSD) detector.

4. Results and discussion

4.1. Single line scanning

The melt pools generated by adjacent laser spots are expected to overlap and create a single wide track due to the arrangement of laser channels in a close-packed array. According to our previous study [5], the melt width of a single laser source was approximately 10% larger than the laser beam size (Full Width at Half Maximum -FWHM), which can be expected due to the relatively slow scanning speed (50 mm/min to 100 mm/min). To evaluate the effect of pitch distance (d_p) on melt pool resolution, two lasers were activated at a laser power of 4.5 W and scanning speed of 100 mm/min. The d_p was varied by activating the two lasers in different configurations by omitting channels within the array and spacing out the lasers used by one period at a time. The channel configurations used in this investigation and the resulting surface morphology of fabricated tracks in Ti6Al4V powder are shown in Fig. 3 (with the dashed yellow circles indicated laser spot position relative to each other). This shows results of lasers 1 and 2 activa-

tion (overlap by 38.1 μm), 1 and 3 (separated centre to centre by 76 μm), 1 and 5 (separated by 153 μm), 1 and 7 (separated by 228 μm), finally 1 and 9 (separated by 305 μm). In general, when the d_p of channels increases, the two molten tracks change from being entirely merged to being completely separate. For values of d_p less than the melt pool width (less than160 μm), formed by activating channels (1&2, 1&3, and 1&5, the melt pools merge together and form a single wide track, with the track width increasing from 125 μm in Fig. 1(a) to 275 μm in Fig. 4(c). A partial separation between the two molten tracks is observed when d_p is increased to 228 μm by activating channels 1&7, as shown in Fig. 3(d). We also note that decreasing the laser pitch increases the surface energy density and therefore influences the melt pool morphology. With an even higher pitch distance (d_p = 305 μm), the two melt pools become completely separated with an unprocessed area of powder ~ 140 μm wide visible between the tracks as shown in Fig. 3(e). The morphology of tracks also changes, from a uniform continuous track when using channels 1&2 to a discontinuous track with defects (unmelted powders, porosity within the single track) when 1&9 were used. The configuration of channels 1&2 results in a preceding laser spot, which indicates that the intensity increases and the time to conduct energy away from the melt pool decreases. The melt pool (that subsequently solidifies to form the track) is strongly influenced by this overlapping effect, with deeper melt pools created as a result of the higher energy densities. The opposite is also true, offsetting the parallel beams so that they are spaced out from each other results in a reduction in the surface energy input (E_s). However, the track width increases because the energy is distributed over a wider area. Zhang et al. [31] studied the effect of increasing the offset between 2 lasers in the lateral direction under different laser power and found that surface energy density is mainly influenced by laser power and hatch spacing. For instance, increasing the laser power from 60 W to 100 W increases the maximum hatch spacing from 140 μm up to 200 μm with a wider merged melt pool. Similarly, a computational study of synchronized multibeam strategies by Heeling et al. [32] found that the melt pool width increased considerably when using a hatch spacing>0.75 times the beam diameter. In this work, it was observed that the width of the melt pool increased significantly for offsets similar to or larger than the diameter of the beam. Therefore, to ensure complete merged melting, from this point forward the investigation is limited to pitch distances less than 153 μm i.e., LP1, LP2 and LP3.

4.2. Single layer scanning

4.2.1. Effect of laser beam profiles

The key processing parameters in LPBF that affect the temporal and spatial energy distribution throughout the process are laser power, scanning speed, hatch distance and layer thickness. Therefore, researchers have combined these parameters into different metrics energy density (linear energy density, surface energy density, and volumetric energy density) to evaluate the effectiveness of parameter-set on the morphology of the samples [33]. In this study, the surface energy density has been used to investigate the effect of laser power, scanning speed and pitch distance (laser profiles) on the melt pool morphology. It is important to gain an understanding of the dimensions of tracks created using an array of lasers, complete layers will be formed by overlap of consecutive scans, this overlap must be optimized in order to prevent defects
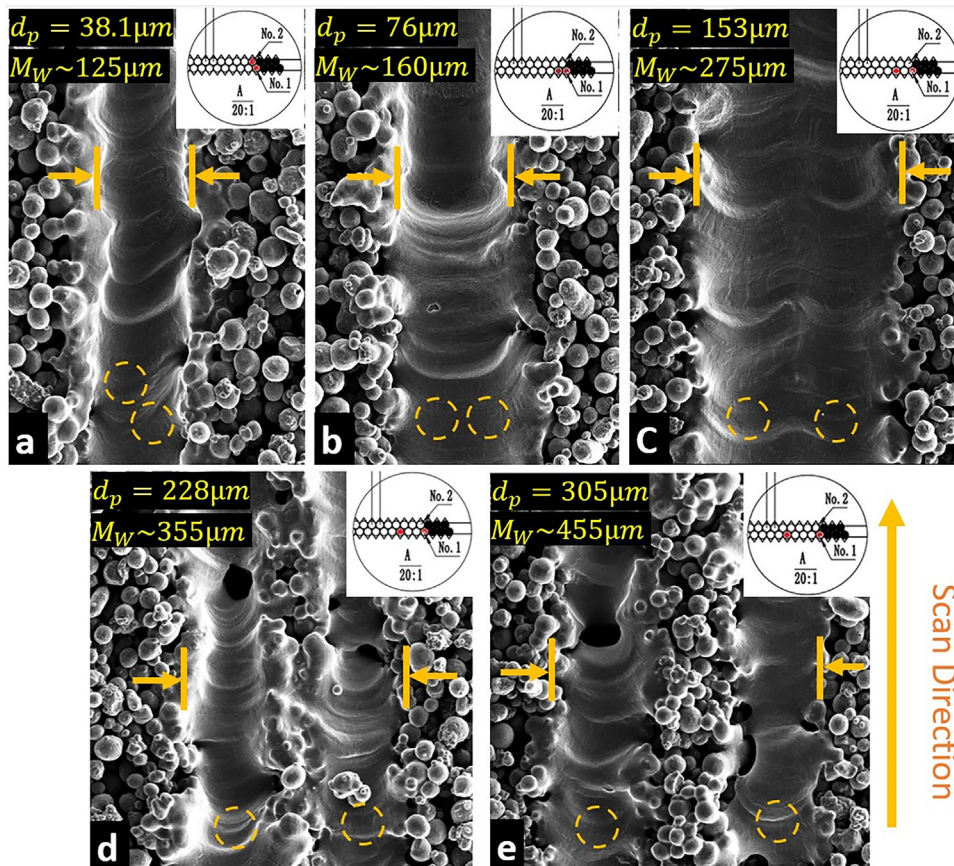
Fig. 3. Morphology of single tracks using two lasers (a) channels 1&2 (d_p = 38.1 μm) (b) Channels 1&3 (d_p = 76 μm) (c) Channels 1&5 (d_p = 153 μm) (d) Channels 1&7 (d_p = 228 μm) (e) Channels 1&9 (d_p = 305 μm).
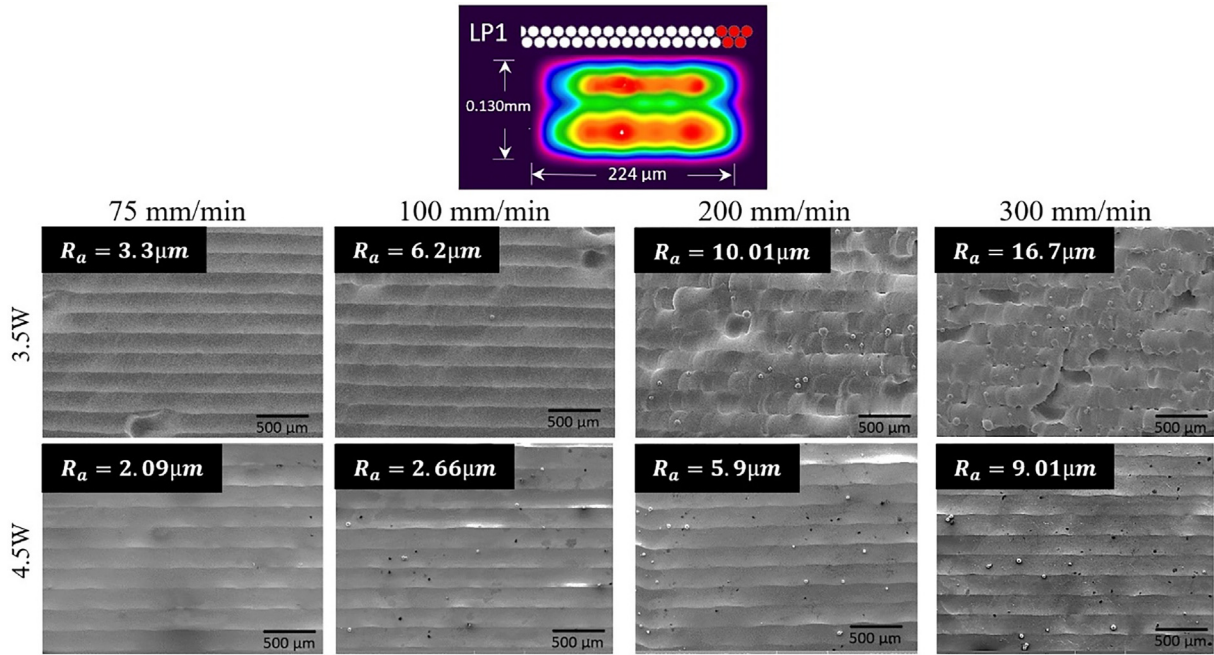
Fig. 4. Surface morphologies of Ti6Al4V under different processing parameters using LP1 configuration (each track was formed using five lasers).

related to excessive or insufficient surface energy input. In contrast to a traditional LPBF system where the track is formed using a single heat source (single laser), the current laser system uses multiple lasers that together create a single wide track for each scan. Figs. 4-6 show the surface morphology using SEM, for a single layer created using five simultaneous lasers under three different beam profile configurations (LP1, LP2, LP3 respectively) as described in Fig. 3. A single layer of 10×10 mm^2 scanning area was fabricated using laser powers of 3.5 W and 4.5 W at varying scanning speeds (75 mm/min − 300 mm/min), where the hatch distance H_d was fixed at 10% of the beam profile. The effect of the laser profile and the associated surface energy input (E_s), is noticeable on the results. Thus, E_s influences the morphology of the layer and the

processing range (laser power and scanning speed). Fig. 4 shows the results for LP1, where the melt pool width of each track created with five lasers is approximately 286 μm. The surface is uniform, and the tracks are consistent and closely merged with each other. The beams within each track form a smooth surface, however between adjacent tracks there is a slight protrusion. The boundary between the tracks is well fused, creating a continuous layer; this is further investigated in the cross-section examination. An average surface roughness (R_a) of 2.02 μm was achieved at 4.5 W and scanning speed of 75 mm/min. This is attributed to the 2D array configuration of LP1, where the second, interleaved row of lasers increases both the surface energy input (E_s) and the interaction time with the melt pool, which reduces the R_a. The results for LP2
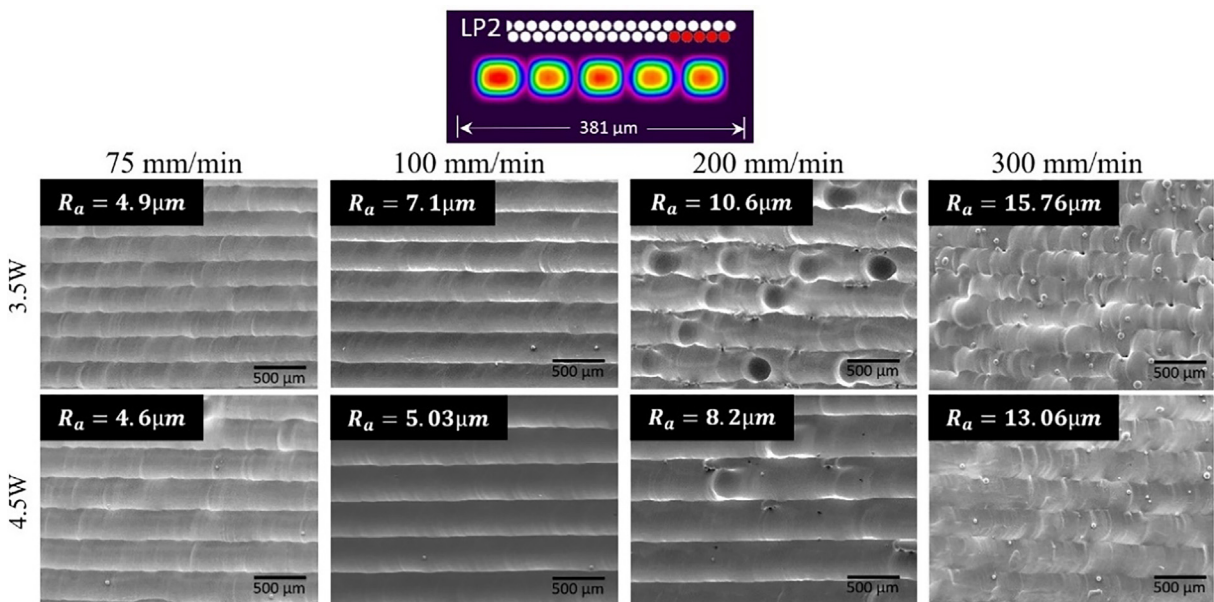
Fig. 5. Surface morphologies of Ti6Al4V under different processing parameters using LP2 configuration (each track was formed using five lasers).
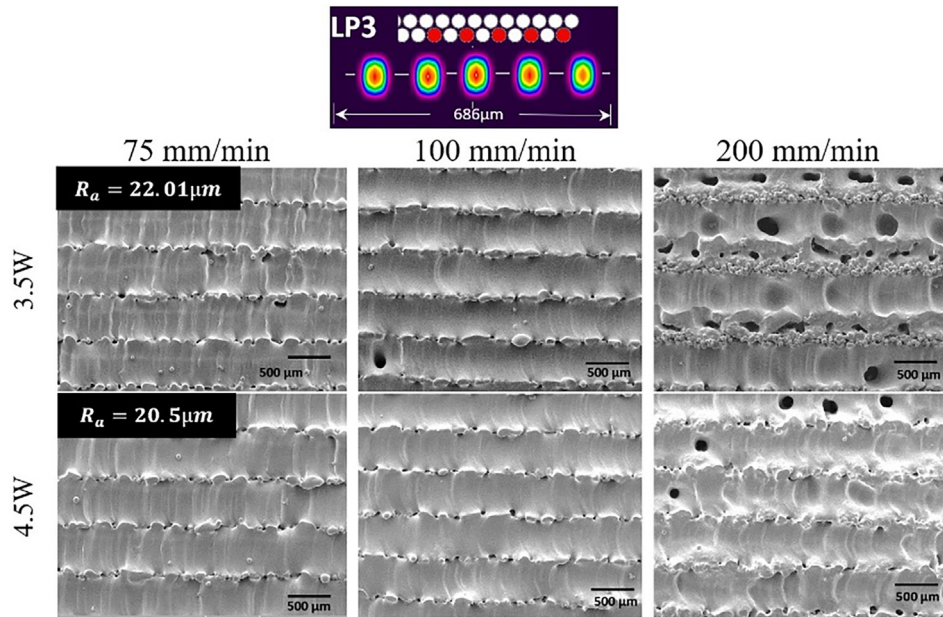
Fig. 6. Surface morphologies of Ti6Al4V under different processing parameters using LP3 configuration (each track was formed using five lasers).

are shown in Fig. 5, showing wider continuous tracks (~405 μm wide) with a smooth top surface similar to LP1. However, the boundary between adjacent scans is more pronounced, indicating a higher surface roughness (R_a = 4.6 μm) compared with LP1. This can be attributed to a reduction in both the surface energy input (E_s) and the interaction time compared with LP1, since for this configuration there is no second row of lasers following the first. The results for LP3 are shown in Fig. 6. Although the use of the LP3 configuration produced continuous single tracks for each scan, the surface energy input (E_s) of LP3 was insufficient to merge adjacent tracks and smooth single layers could not be produced. This resulted in incomplete overlap and defects (un-melted particles), which affect the morphology resulting in a high surface roughness, R_a= 20.5 μm. Therefore, LP3 cannot successfully form single layers and is deemed unsuitable for multilayer parts.

Fig. 7 shows the cross-section, observed by SEM, of single layers generated in Ti6Al4V using LP1, LP2, LP3 scanning strategies. The scanning speed was fixed at 100 mm/min with varying H_d between the scans at 10%, 20% and 30% of the melt pool size in order to evaluate the influence of H_d on melt pool morphology. LP1 produced a melt pool depth d_m of 180 μm for H_d = 250 μm, with a high-density smooth surface. As the H_d was increased the depth increased slightly to 194 μm and 188 μm for H_d = 200 μm and H_d = 150 μm,

respectively. The cross-section for LP2 shows a wave-like surface structure for 10% overlap. The track depth decreased to 168 μm for H_d = 350 μm compared to LP1. However, as the H_d was reduced the surface roughness reduced whilst the melt pool depth increased to 174 μm and 179 μm for H_d = 300 μm and H_d = 280 μm, respectively. These results indicate that the layer depths and the average R_a improve by reducing the H_d. For LP3, the melt pool depth was less than 100 μm for all conditions. Weak bonding and inconsistent tracks were observed. This is due to the distribution of energy over a wider range perpendicular to the scanning direction, forming a wider track with incomplete overlap as already described. The maximum melt pool depth is strongly affected by this phenomenon since the recoil pressure increases with increasing intensities [32,34]. Yadroitsev *et al.* claim that the reduction in track height observed in their work was due to denudation phenomena [35]. The first scan pulls powder towards the melt pool from neighbouring regions, thereby leaving insufficient powder for the following scan and consequently creating a defective layer. Similar results have been reported by Tsai *et al.* [36]. These observations inform us that it is not preferable to employ pitch distances corresponding to double the beam diameter or>10H_d% of the melt pool width to ensure satisfactory surface quality with high throughput performance.
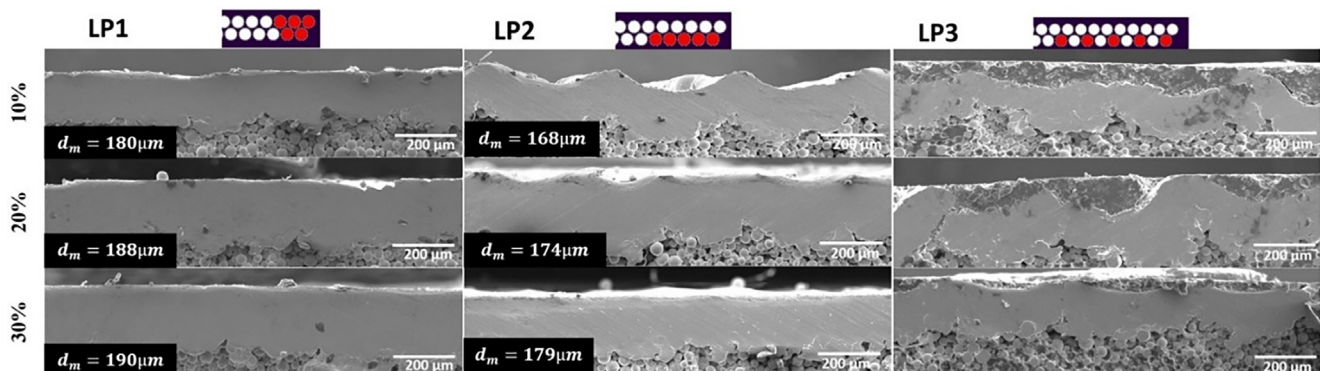
Fig. 7. Cross-section morphology for a single layer produced using LP1, LP2, and LP3 at laser power 4.5 W with scanning speed of 100 mm/min.

Table 1 provides a comparison of the processing performance of a single beam with the various multi-laser array configurations used to fabricate single 10 × 10 mm^2 area layers at 4.5 W, 100 mm/min (optimal parameter for all profiles). Scanning times using LP1, LP2, and LP3 are 5, 9 and 15 times faster than for the single diode laser. Upon future upscaling of the LP1 array to x50 lasers, the scanning time is predicted to be x88 faster than for a single traversing diode laser. These results demonstrate that LP1 and LP2 scanning configurations could be used to enhance processing quality and throughput with the option of scaling to large arrays.

4.2.2. Effect of laser power and scanning speed

Whilst laser power and scanning speed are explicitly linked to energy density, the effect of laser power is more evident on surface morphology (porosity/surface roughness) and the processing window, whereas the scanning speed significantly influences melt depth (as shown in Fig. 8). For all configurations, increasing laser power from 3.5 W to 4.5 W is observed to improve the processing performance, whilst the effect of scanning speed is more dominant on the depth. For instance, when a laser power of 3.5 W was used, a low surface roughness appeared at a 200 mm/min scanning speed for all laser profiles, as was shown in Figs. 4-6. However, increasing the laser power to 4.5 W improved the processing window to allow for scanning speeds in excess of 300 mm/min for LP1 and 200 mm/min for LP2. In general, the results show that increasing the laser power and/or reducing the scanning speed will increase the surface energy input (E_s), and therefore the melt pool depth (and hence thickness) of the fabricated layer. For LP1, the optimal surface energy density results in high density at scanning speeds ranging from 75 mm/min up to 200 mm/min and 75 mm/min up to 300 mm/min for 3.5 W and 4.5 W, respectively (as can be determined from Fig. 5). At a 75 mm/min scanning speed, a maximum melted layer thickness close to 220 μm was achieved using laser power of 4.5 W. In comparison, LP2 formed a fully dense layer at a scanning speed up to 100 mm/min and 200 mm/min for 3.5 W and 4.5 W laser powers, respectively (Fig. 5). LP2 produced a maximum thickness of about 190 μm under similar processing conditions to LP1. LP3 did not show a significant improvement when increasing the laser power from 3.5 W to 4.5 W, as evidenced in Fig. 6. For LP3, smooth continuous single tracks are formed when traversing the multi-laser beams at speeds slower than 100 mm/min, whereas bonding defects appear between the tracks at faster speeds. However, it should be noted that the reduction in surface energy density (when using LP3) is due to the wide pitch distance. Scanning speed not only dictates the melt pool depth but also influences the surface finish. Fast scanning speeds above 200 mm/min produce spatter on the surface, which causes uneven powder spreading in subsequent layers thus effecting multi-layer parts. This phenomenon is more common when two adjacent lasers are used in the LPBF process [19,36]. Since 4.5 W provides excellent surface properties, high density and higher productivity compared to 3.5 W, 4.5 W was selected to produce the multi-layer parts for the remainder of this study.

4.3. Normalized processing windows for Ti6Al4V (multilayer)

A total of 15 experiments were performed using ten lasers in LP1 and LP2 configurations. These experiments cover the range of process parameters within the limits given in Table 2 to identify the optimal processing window for Ti6Al4V by evaluating the density of the specimens. It is known from previous studies conducted by Thomas et al.[29] and Jiang et al.[37] that laser power and scanning speed are the key determinants of part density in SLM. For this reason, a maximum laser power of 4.5 W was used, while the energy input was controlled by varying the scanning speed only. Furthermore, the effect of overlapping of adjacent beams/melt pools influences process efficiency; increasing the hatch distance improves the production rate. Therefore, based on our single-layer study (section 4.2.1), the investigators opted to fix the hatch distance at 10% of laser width, which is sufficient to obtain a good overlap.

LPBF of Ti6Al4V has been extensively investigated using 1070 nm lasers with one study using 808 nm [5]. However this prior work has primarily used single beam sources [38] or a maximum of two beams (preceding or beside each other) [32]. Our current research uses multiple laser beams. We have attempted to extract and normalize processing parameters from the literature in order to provide a simple starting point for optimisation of appropriate processing windows. Normalization has been carried out by Thomas [29] for EBM. A sufficiently detailed explanation of the processing was provided, which we were able to adapt in our previous research for normalization of laser parameters for a single-source laser [5]. The fundamental concept of normalization is to compare the actual energy over the minimum energy input for complete melting, keeping the material properties in mind, as defined by Equation (1).

$$E^* = \frac{P^*}{v^* l^*} = \frac{AP}{2vlr\rho C_\rho(T_m - T_0)} \tag{1}$$

The normalized volumetric energy density E^* obtained by calculating the normalized primary parameters P^*, v^*, h^* and l^*, where A is the material absorption at the wavelength of lasers used in the current work (808 nm), ρ is the material density (kg m^{-3}), C_ρ is the specific heat (J kg^{-1} k^{-1}), v is the scanning speed (m), T_0-ambient temperature (K), T_m-powder bed temperature (K) and r-beam radius (m). However, since this research uses a unique multi-beam configuration during the process, modification of the equation is required in order to calculate the normalized energy input for the overlapping multi-laser beams compared to a single laser. In Equation (1), Thomas et al. [29] considered the length of the beam, represented by 2r, which defines both the width of the scan and the scan area. This is not applicable for multiple beams, in which the entire beam length delivers the energy, and thus r is replaced by the length of the beam as described by Equation (2).

$$r = (n * 2r_b) + ((n - 1) * d_g) \tag{2}$$

Where n is the number of lasers, r_b is the radius of a single laser, and d_g is the separation distance between lasers. This expression covers the LP1 and LP2 laser arrays used in this study. Thus, the

Table 1
Comparison between a single laser and multi laser array 4.5 W, x5 lasers approach for single layer (10 × 10 mm^2).

Scanning Profiles	Laser scanning width (μm)	Hatch Distance (μm)	Scanning length (mm)	Scanning time (sec)@100 mm/min	Faster
x1 single laser	65	40	2500	1500	–
LP1 (x5 lasers over two linear arrays)	224	200	500	300	x5
LP2 (x5 lasers over one linear array)	300	300	285	171	x9
LP3 (x5 lasers over one linear array)	400	400	98	98	x15
x50 laser arrays (1D)	3800	3400	17	17	x88
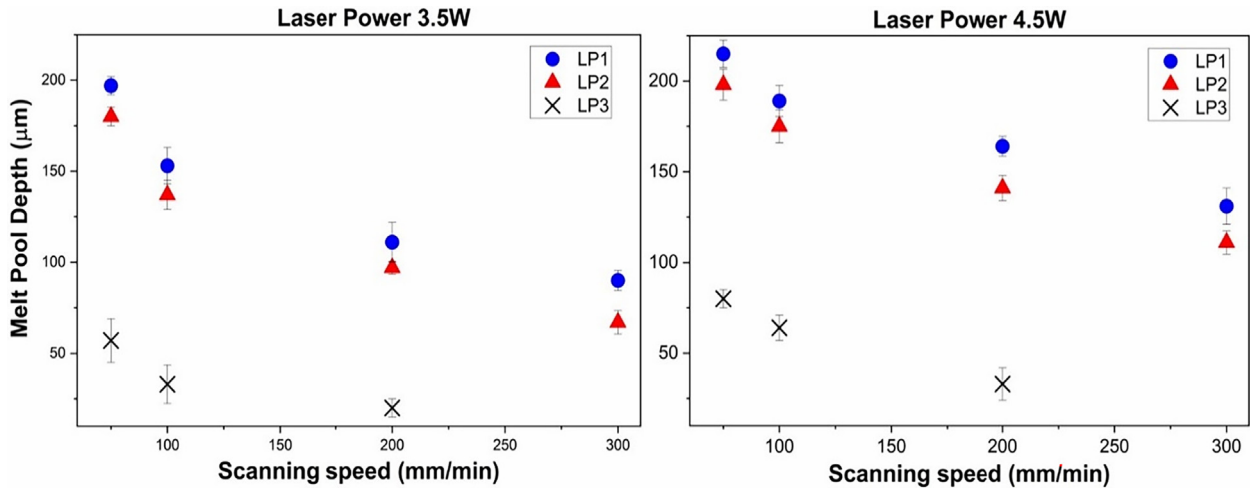
Fig. 8. Effect of laser power and scanning speed on melt pool depth for 3.5 W and 4.5 W laser powers.

Table 2
Processing parameters and thermophysical properties of Ti6Al4V used to normalize energy density.

Processing Parameters	Units	LP1	LP2
Laser power (P)	W	4.5	
Scanning speed (v)	mm/min	75–600	
Scanning width (r)	μm	762	414
Hatch distance (H_d)	μm	685	372
Layer Thickness (l)	μm	70	
Physical Properties of Ti6Al4V at 1604 °C			
Specific heat capacity ($C\rho$)	(K Jg^{-1}K^{-1})	526	
Melting Temperature (T_m)	(°C)	1604	
density (ρ)	(Kg/m^3)	4430	
Thermal diffusivity	(m^2/s)	6×10^{-60}	

Fig. 9. Normalized energy input showing the location of the experimental parameters and the optimal region for LP1 and LP2.

diameter has been redefined by the length and the irradiated area is composed of the sum of all active beams and does not depend solely on the radius of a single beam. Similarly, the total energy input is the sum of the energy input from all active beams. This modified equation caters for the multi-beams, the effect of pitch distance, the effect of the number of the active beams and is directly applicable to scaled up models. Fig. 9 shows the normalized processing diagram representing normalized energy density E* (on the x-axis) and normalized hatch h* (y-axis) on a log$_{10}$ scale. The isopleth dashed lines represent the minimum energy input E_0^* required to melt the material at a specific volume $2rl^*$. In general, the green area within the range of $4.5 \leq E^* \leq 14.8$ represents the normalized processing parameter that results in high-density parts (>95% density). The use of processing parameters that give an energy density within the red zone defined by E* > 14.8 leads to excessive energy, causing material vaporisation. In contrast, a lack of fusion occurs when employing a combination of processing parameters that provide E_0^* less than 4.5 (i.e within the blue region). Here the energy is insufficient to melt the powder between layers causing the density to drop below 90%.

4.4. Density evaluation

In this study, the parameters that hold the main influence on part density are the pitch and the scanning speed. Fig. 10 illustrates the variation in density according to E_0^* and the corresponding scanning speed for LP1 and LP2. At E_0^* of 7.3, both profiles provide a maximum density of 97.8% for LP1 (at a speed of 300 mm/min)

and 96.7% (at a speed of 200 mm/min). LP1 produces higher density (>95%) at higher speeds within the range of 150 mm/min to 500 mm/min compared to LP2, for which high density parts are only possible in the range between 100 mm/min to 300 mm/min. This is due to the smaller pitch in LP1 that significantly increases energy input, thereby improving the density of the part while improving the process efficiency. Fig. 11 plots part density as a function of normalised energy density, E_0^*, for LP1 and LP2. For both configurations, part density increases initially with increasing E_0^* by reducing the scanning speed. However, the density begins to decrease when $E_0^* > 14.8$ due to excessive energy input, which causes the samples to warp and distort making the parts unacceptable. In contrast, increasing the scanning speed moves E_0^* into the "insufficient" region (E_0^* less than 4.5) where the density falls sharply to less than 90% due to improper melting, lack of fusion and weak bonding between layers. It is important to note that using a combination of processing parameters to give similar E_0^* for LP1 and LP2 does not guarantee the same sample density, as each sample has a different thermal history [38] as influenced by the laser configuration (pitch distance) used. A similar conclusion has been reported in [37]. Fig. 11 and Fig. 12 show the cross-sections of multi-layer parts for LP1 and LP2 respectively and the variation of density with E_0^* and corresponding scanning speed.
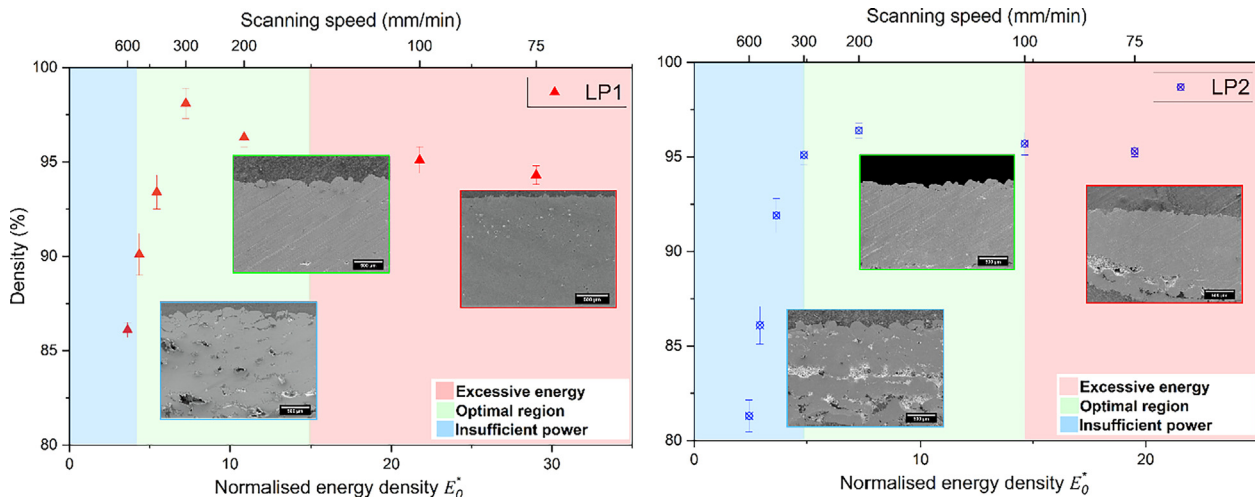
Fig. 10. Variation of density with speed and normalised energy density for LP1 and LP2.
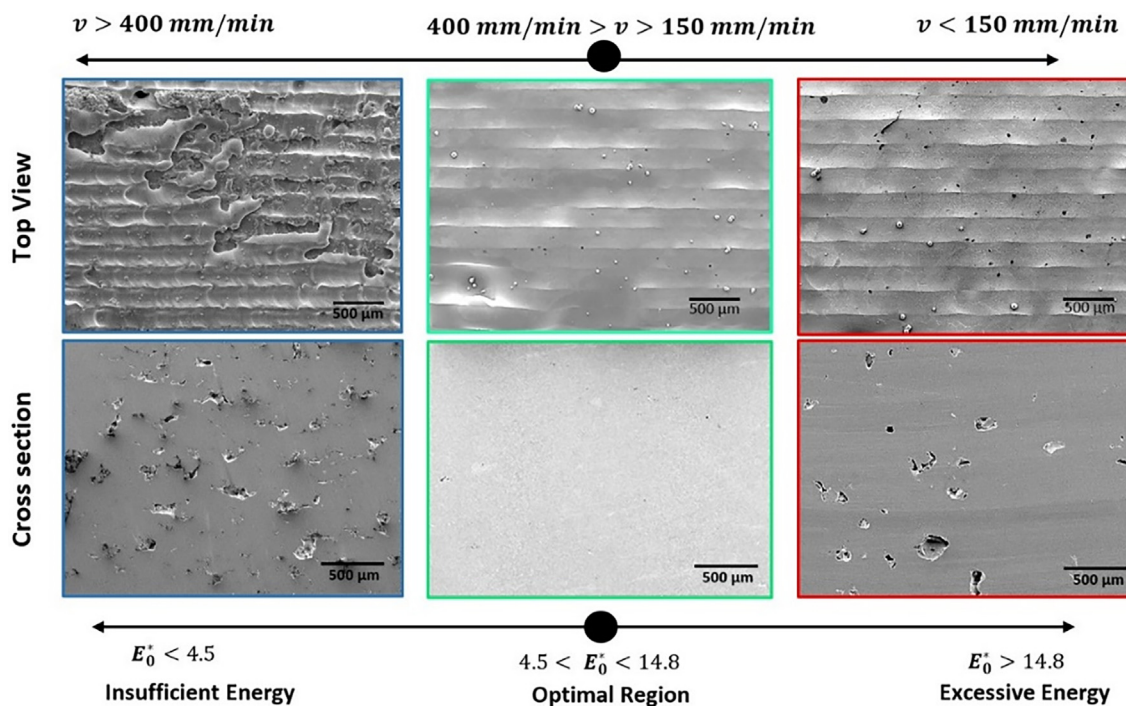
Fig. 11. The effect of scanning speed on the top surface and cross-section for LP1.

4.4.1. Surface roughness

Fig. 13 shows 3D optical microscope images for multi-layer parts processed at different speeds using LP1 and LP2 configurations at a power of 4.5 W, for which variation of the top surface roughness can be observed and root mean squared surface roughness, R_a extracted. The laser power, scanning speed, and hatch distance are known to affect the surface roughness, with laser power and hatch distance reportedly having the greatest influence [37]. In our case, the pitch (similar to hatch distance in the single beam LPBF process) for LP1 and LP2 is different and dictates the power density. We have seen already that LP1 has a higher energy density compared to LP2. For both LP1 and LP2 configurations, R_a is observed to increase with an increase in speed. For 75 mm/min, R_a is minimal for both LP1 and LP2 at 7.1 μm and 8.6 μm, respectively. The surfaces are smooth and there are no visible striations or protrusions. However, the roughness for LP2 is generally higher than that of LP1 and even though R_a increases with speed at 300 mm/min, LP1 has 21% lower roughness than LP2, perhaps as a result of a re-melting effect that may be generated as a result of activation of the second linear array within the laser head. All parameters that produced densities>95% were analysed for R_a, and generally LP1 has approximately 17–21% smoother surface than LP2. Energy density varies as a function of both speed and beam profile, consequently affecting the melt pool dynamics and resulting in a variation in surface R_a. Both LP1 and LP2 have different power densities due to their particular beam configurations. In general, slow scanning speeds (less than 100 mm/min) reveal that higher energy densities produce more consistent melt pools (e.g. fully formed, consistent overlap) under multi-laser irradiation, with an almost "top-hat" energy distribution. In contrast, the lower energy input at higher speeds lead to spatter and particles that cause higher R_a. Similar findings have been reported in the litera-
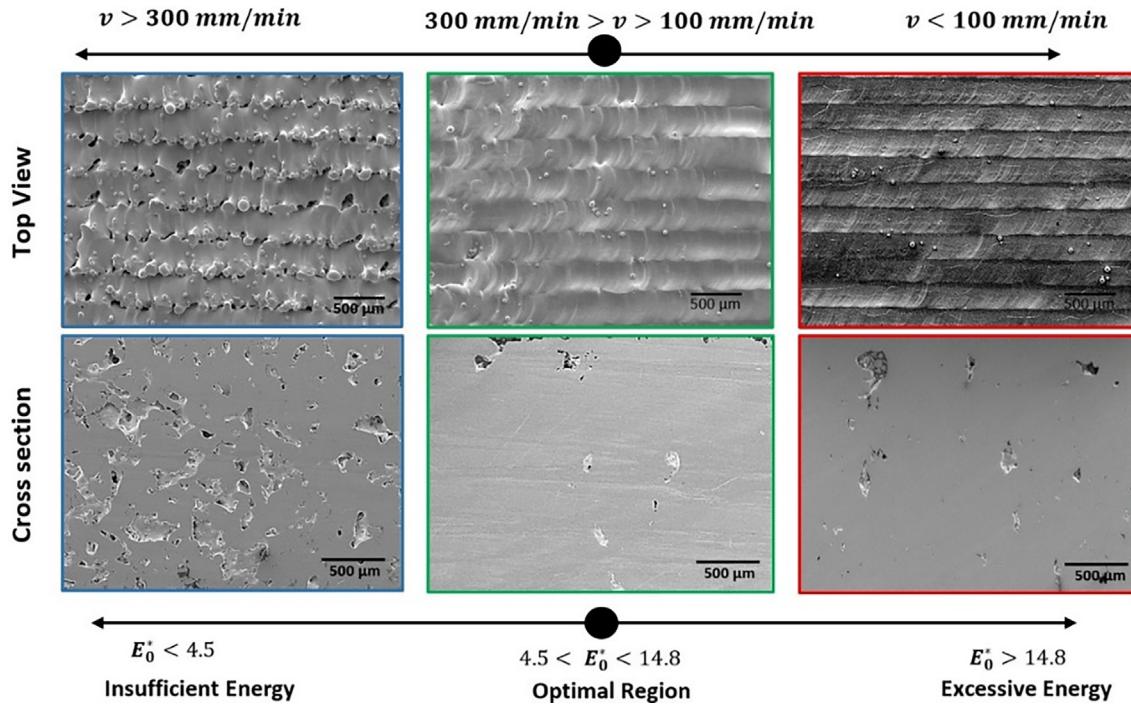
$v > 300 \, mm/min$ $300 \, mm/min > v > 100 \, mm/min$ $v < 100 \, mm/min$

Top View / Cross section

$E_0^* < 4.5$ — **Insufficient Energy**

$4.5 < E_0^* < 14.8$ — **Optimal Region**

$E_0^* > 14.8$ — **Excessive Energy**

Fig. 12. The effect of scanning speed on the top surface and cross-section for LP2.

75 mm/min   100 mm/min   200 mm/min   300 mm/min

LP1: Ra=7.1µm, Ra=8.1µm, Ra=10.6µm, Ra=13.4µm

LP2: Ra=8.6µm, Ra=10.1µm, Ra=12.1µm, Ra=15.6µm
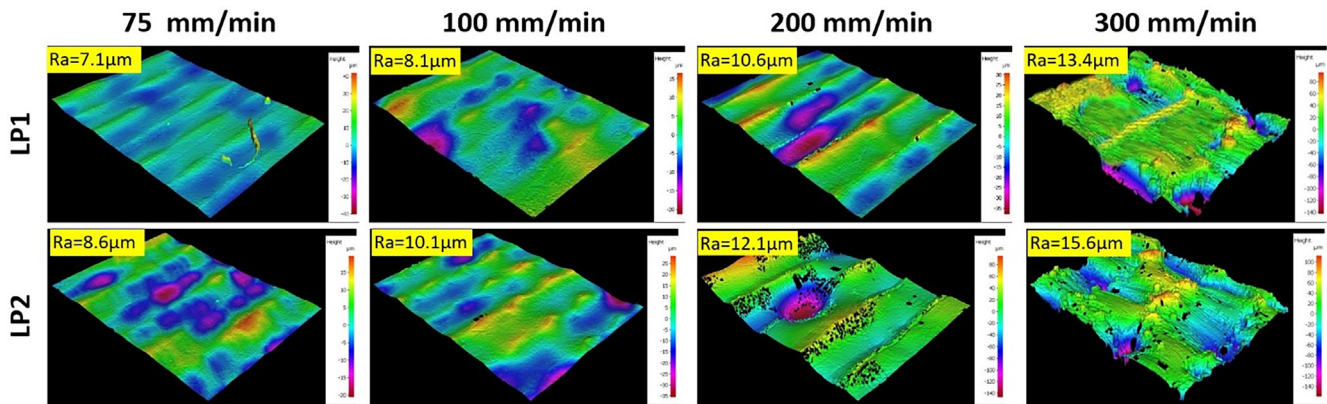
Fig. 13. Surface roughness for different speeds and profiles, with corresponding r.m.s roughness R_a.

ture, where low energies tend to lead towards balling of melted powder and porosity [37].

4.5. Microstructure

Only specimens with a density of > 95% were analysed, confined to processing speeds between 75 mm/min and 300 mm/min. The cooling rate is known to be a key factor in influencing the microstructure of Ti6Al4V in the LPBF process. The continuous cooling transformation has shown that microstructure formation can be controlled by controlling the cooling rate above the β transus (994 °C), explained in detail by Ahmad and Rack [39]. The cooling rate during the process can be controlled by heating the chamber/powder bed or by adjusting processing parameters such as the hatch distance and/or processing speed. Our previous study demonstrated that slow scanning speed combined with low laser power can help to reduce the cooling rate, providing the ability to develop a β phase. This capability is not a common capability of traditional LPBF processes. Fig. 14 illustrates the effect of beam

configuration (LP1 and LP2) and scanning speed on the microstructure with SEM images of the top surface of samples produced at various speeds using LP1 and LP2 at a fixed laser power. It can be seen that both profiles produce samples with dominant (α/β) microstructure. However, the effect of the beam profile on the coarseness of the α/β transformation is more pronounced than that of scanning speed. Above 100 mm/min, both profiles produce a fine (α/β) Widmanstätten, composed of α lamellas and a small amount of β phase due to the relatively rapid cooling rate. In contrast, samples produced at scanning speeds below 100 mm/min are composed of coarse (α/β) Widmanstätten. Due to the second laser array in LP1, which maintains the temperature above the β transus for a longer period of time than LP2, the cooling rate is reduced and a coarser microstructure is observed. Fig. 15 shows the temperature transient measured using a pyrometer for LP1 and LP2. The temperature rise is similar for both configurations; however, differences can be observed in their cooling rates. It takes 0.67 s for LP1 to maintain the temperature between the $T_{\beta \, transus}$ = 994 °C and martensite temperature T_{ms} = 575 °C compared to 0.37 ms
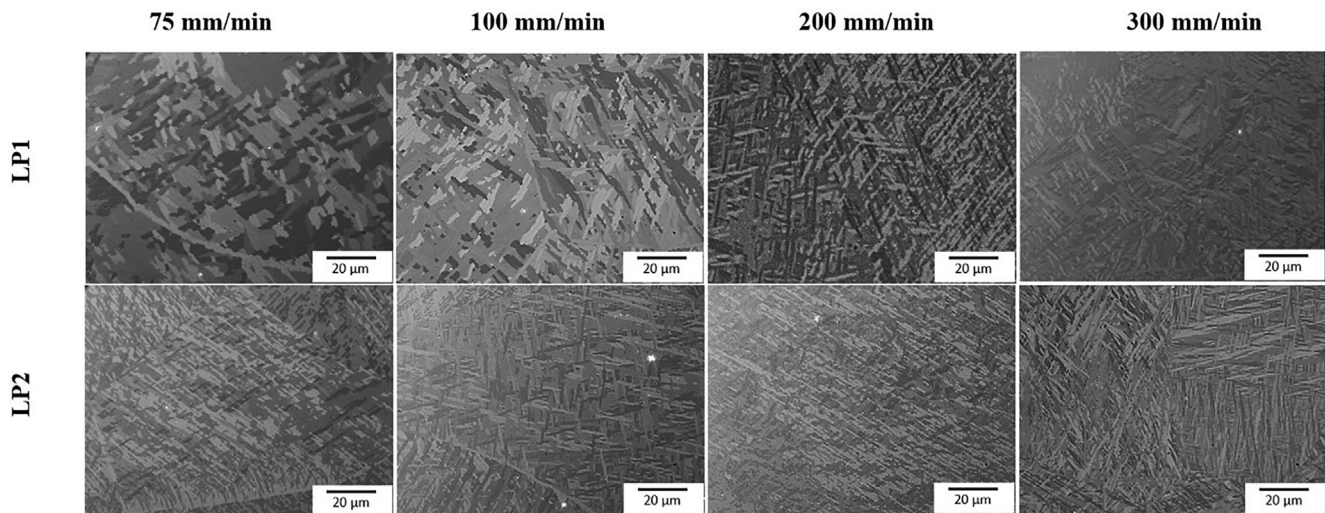
Fig. 14. Ti6Al4V microstructural variation with speed and laser beam profile.
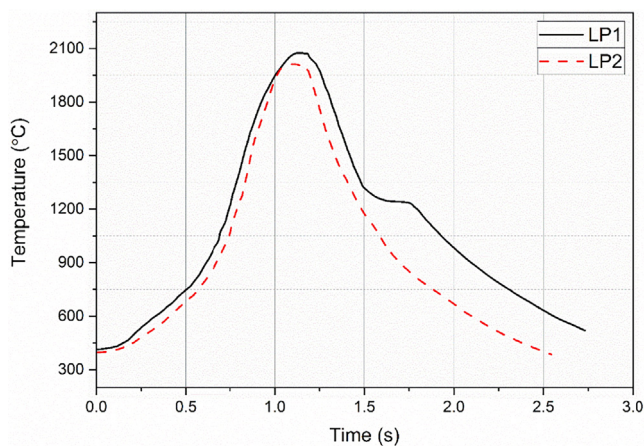
Fig. 15. Temperature comparison at scanning speed of 75 mm/min for LP1 and LP2.

for LP2. Therefore, the average cooling rate for LP1 was 600 °C/s compared with a 1086 °C/s for LP2. This is consistent with the results of the microstructure reported in the literature.

Further investigation has been conducted to evaluate the texture of the top surface of the samples (xy) to understand the effect of the beam profiles and the scanning speed during the process using electron backscatter diffraction (EBSD). EBSD has been carried out on an area of 809 μm × 606 μm with a step size of 0.5 μm. Fig. 16 shows the colour inverse pole figure (IPF), which confirm a basketweave-like α–β microstructure observed inside the prior-β grains under all processing condition. The scanning speed has more influence on the crystallographic texture than the laser profiles. As shown in Fig. 16, at scanning speed of 75 mm/min, a columnar β-grains of whereas at 200 mm/min exhibits fine equiaxed β grains. However, the average grain size (AVG) was larger using LP1 (4.3 μm) than LP2 (3.7 μm) at low speed. When the Ti alloy is heated for a significant time above the β grains, the grains tend to increase in size where processing below the β grains will not change the grains as the α impedes the movement of β grain [40]. This is true when using LP1, which provides a significant surface energy density than LP2, as discussed previously. From the pole figures(Fig. 17), α texture is weaker than the texture of the high temperature β phase. there is an apparent preference for α phase exhibits a clear crystallographic orientation

of strong preferred orientation less than 0001 > under all processing parameters. The samples produced using LP1 has stronger α phase texture (about 26 times of random) compared with LP2. As the scanning speed was increased, the texture of the α phase got weaker and more random. For LP1 and LP2, the maximum intensity of the texture reduced to 21.28 and 7.59, respectively. In case of β phase, it was found at low scanning speed tend to form a strong crystallographic orientation on ⟨100⟩ and minor on ⟨111⟩. LP1 shows stronger β phase texture than LP2 (about 38.40 compared to 26.26). Increasing the scanning speed weaker the β phase texture and changing the orientation to ⟨111⟩. This is owing to the greater proportion of α phase at high scanning speed, which has a more random crystallographic orientation due to the relatively large number of α variations included inside each β grain [41,42].

4.6. XRd

X-ray diffraction (XRD) can be used to confirm the existence of α/β in the samples produced by LP1 and LP2. Fig. 18 plots the XRD response for LP1 and LP2 at different speeds for 4.5 W lasers. All peaks in the graph have been identified as (α/ά); this is because (ά) and (α) share the same hexagonal closed pack crystal structure, making it difficult to differentiate between the peaks. At 2θ = 35-39°, a diffraction peak can be observed, corresponding to the β (110) phase. This is true under all scanning speeds for LP1 and LP2. However, the peak intensity changes when the scanning speed and laser profiles are varied. For LP1, the β peak shifts to lower 2θ angles at scanning speed less than 200 mm/min. The β phase (200) at 2θ = 57° was only observed at 75 mm/min, which is not common for LPBF processes. This is due to the second array, which has higher energy input and allows more time for ά to dissolve and form the β phase with coarser microstructure, consistent with the microstructure observed using the optical microscope. In general, the peak intensities of LP1 are higher than LP2, which correlates with a finer microstructure observed in LP2. For LP2 at scanning speed above (200 mm/min), the XRD patterns do not change significantly. At scanning speeds below 100 mm/min a slight shift is observed in both the α and β peaks to lower 2θ angles, indicating a transformation from ά to β. Slow scanning speeds lead to a relatively reduced cooling rate, which gives time for ά to transform into the α/β phase. In addition, the slight reduction in the ratio of ά/α peaks indicates a higher volume fraction of β phase in the samples, as suggested by Qiu *et al.* [43].
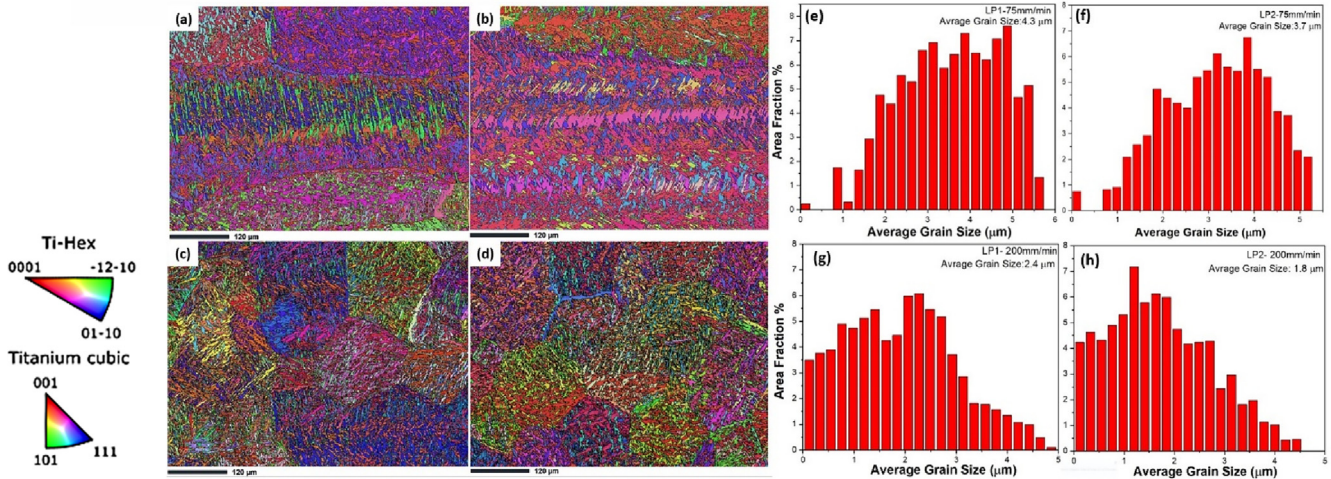
Fig. 16. EBSD analysis of XY-plane from the samples at processing parameters (a) IPF for LP1 at 75 mm/min (b) IPF for LP2 at 75 mm/min (c) IPF for LP1 at 200 mm/min (d) IPF for LP2 at 200 mm/min (e) AVG for LP1-75 mm/min (f) AVG for LP2-75 mm/min (g) AVG for LP1-200 mm/min (h) AVG for LP2-200 mm/min.
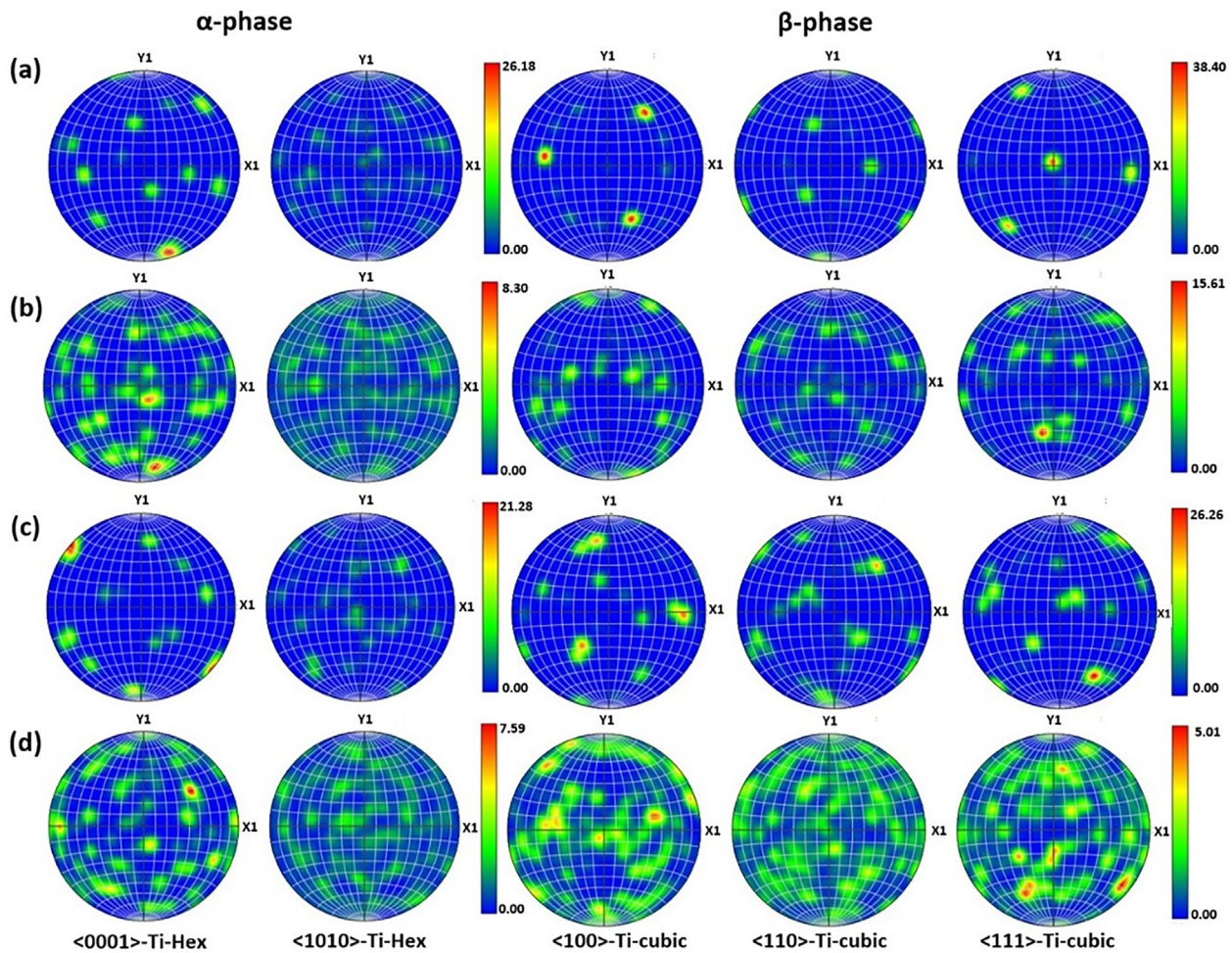
Fig. 17. Corresponding pole figure (a) (PF) for LP1 at 75 mm/min (b) (PF)for LP1 at 200 mm/min (c) (PF)for LP2 at 75 mm/min (d) (PF)for LP2 at 200 mm/min.

4.7. Nanoindentation

This section investigates the hardness and elastic modulus of fabricated samples using the nanoindentation technique suggested by Fischer-Cripps [35]. Hardness is mainly affected by the solidification process, i.e. the cooling rate affecting the microstructure. A reduction in hardness is associated with a coarser microstructure, which is significantly influenced by the processing parameters (pitch distance and scanning speed) used [29]. When the number of structural boundaries per unit volume of material is reduced (i.e. when the grain size is large), the distance over which dislocations can glide before hitting a grain boundary increases. Conse-
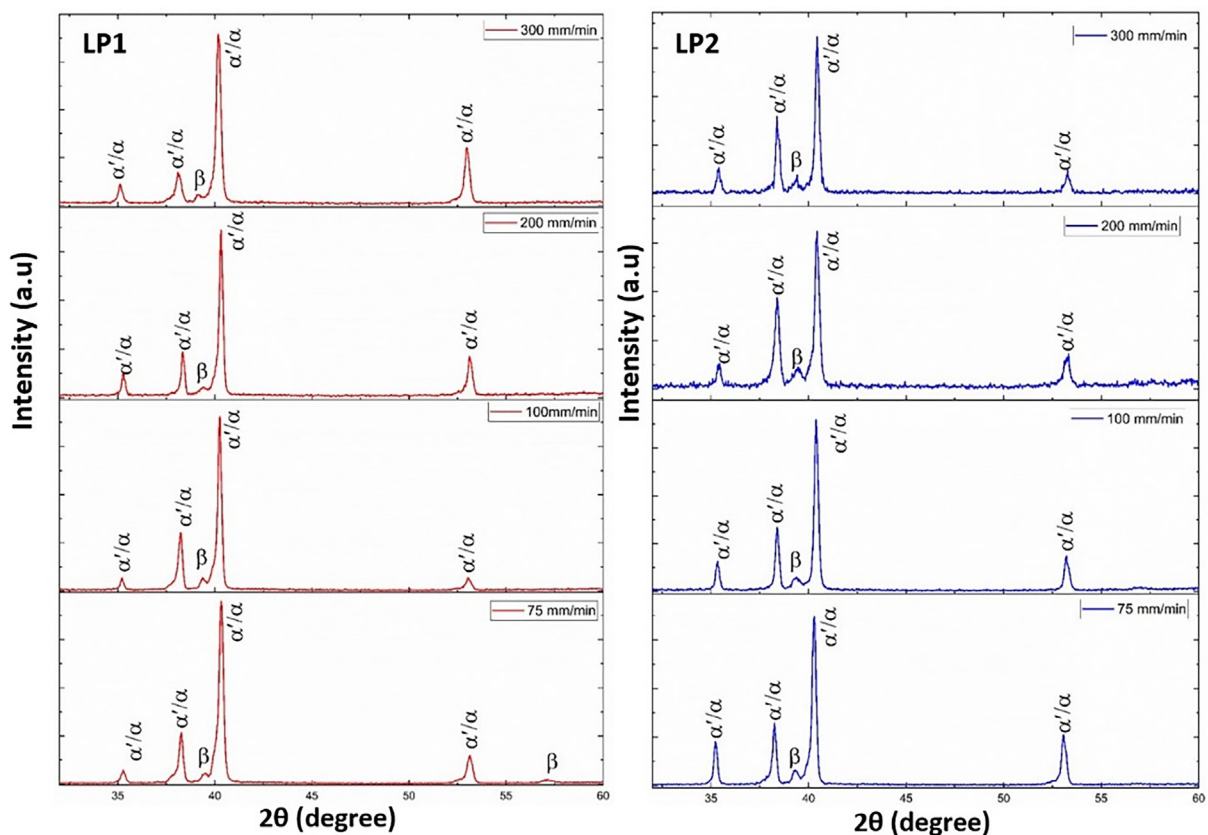
Fig. 18. XRD graphs for LP1 and LP2 at different speeds using 4.5 W.

quently, there is a reduction in material hardness. The results from nanoindentation measurements conducted on samples produced using LP1 and LP2 are shown in Fig. 19 and Fig. 20. These results show hardness to range between 4 GPa and 5 GPa over the range of scanning speeds studied, whereas the elastic modulus is in the range of 110 GPa and 120 GPa. This is similar to the findings of Thijs *et al.* [44], who report the hardness of Ti6Al4V to be between 3.70 and 4.69 GPa with an elastic modulus of 107 GPa for parts manufactured using LPBF. Facchini *et al.* demonstrated a relative hardness of EBM samples around 3.2–3.5 GPa with an elastic modulus of 118 GPa [45]. Furthermore, Cai *et al.* [46] reported hardness varying from 4.0 to 5.5 GPa, depending on the indentation depth. For LP1 the average nano hardness at a scanning speed of 75 mm/min and 100 mm/min was 4.1 GPa and 4.5 GPa, respectively, and the corresponding elastic modulus was measured to be 119 GPa and 118 GPa. LP2 produced a sample with an average nano hardness of 4.5 GPa and 4.8 GPa at a similar scanning speed to LP1. The elastic modulus was 112 GPa and 110 GPa, which is comparatively less than for LP1. At scanning speeds above 100 mm/min, the change in average nano hardness and elastic modulus was negligible as there was no significant change for both profiles. The effect of the beam profiles on the hardness is more
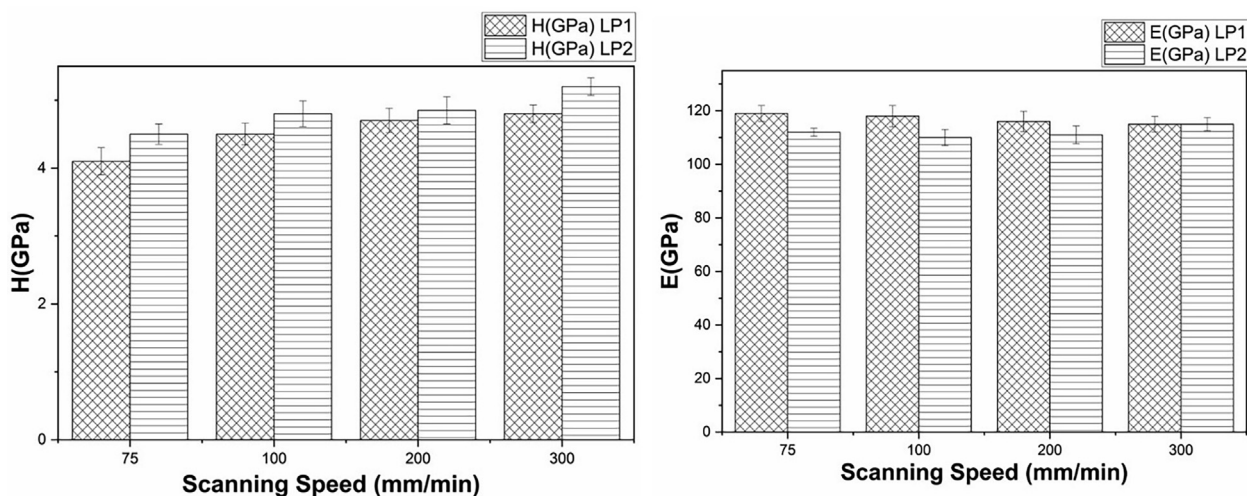
Fig. 19. Nano hardness and elastic modulus comparison for LP1 and LP2 at different scanning speed.
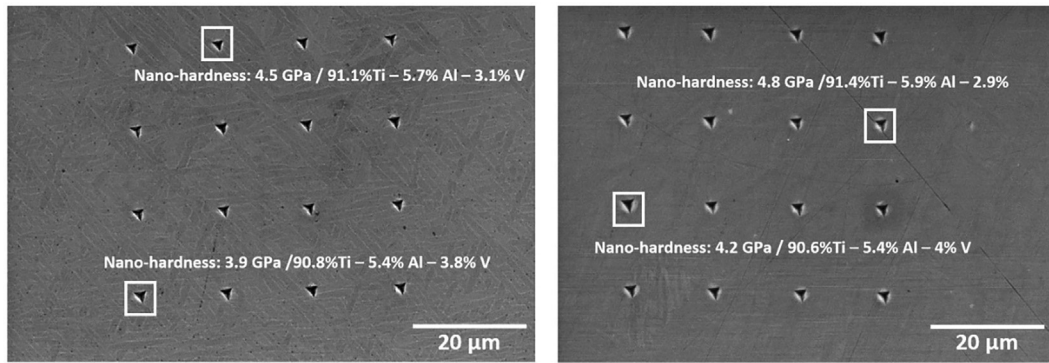
Fig. 20. Nanoindentation and material composition for LP1 and LP2 at 75 mm/min.

pronounced than the scanning speed, with a modest overall reduction. The hardness of samples produced at a scanning speed of 75 mm/min for LP1 is less than of LP2, correlating to the coarser microstructure, as discussed previously. This is consistent with the work reported by Thomas *et al.*[29], which concluded that pitch distance is the principal factor in controlling the hardness of the alloy. This is the case in our study, particularly for LP1 in which the overlap between adjacent spots is 50%.

Fig. 21 plots the load, P as a function of displacement, h (the P-h curve) for indentations performed on samples produced using LP1 and LP2 at 75 mm/min. The curves show a more significant penetration depth in LP1 (coarser microstructure) compared to LP2. The penetration depth varies between 230 and 265 nm for samples made using LP1 compared to average penetration depth of 235 nm for samples made using LP2. This could be attributed to indentation made at different phases, as shown in Fig. 20. When the indenter is interacting with the LP1 sample, the P–h curve shows a higher depth value than LP2 (Fig. 21), indicating that the microstructure of the LP1 sample is softer than LP2. The indentation that occurred over α/β lamellas has a higher depth compared with the α- phase region, as it is well known that α-phase is harder than the α/β phase. A similar conclusion has been reported in the literature [47]. The results confirm that the second laser array and the pitch distance significantly influence the microstructure and the mechanical properties of Ti6Al4V.

Further investigation of the composition was carried out using EDS to determine the specific concentrations of aluminium and vanadium in the alloy, since the concentrations of these elements is known to play a significant role in phase transformation. Vanadium is widely known to stabilize the β-phase, whereas Al is associated with the α-phase. Fig. 20 does not show any evidence of significant variation in aluminium and vanadium elements for either sample set. This indicates that the transformation of phases is not influenced by a variation in alloying elemental composition but, significantly for this study, it is determined by the cooling cycle.

5. Conclusions

This investigation has shown that a fibre coupled, multi-laser DAM methodology presents a viable, efficient and scalable alternative to traditional LPBF approaches, offering new process thermal control and capability through selection of scanning laser beam profiles. High powder bed temperatures were recorded, sufficient to melt Ti6Al4V using low power 4.5 W diode lasers operating at a more efficient wavelength (808 nm) compared to standard LPBF, improving laser absorption by 14% for Ti6Al4V powder. A normalization model was developed for the multi-laser system, it was found that for E_0^* in the range of 4.5 to 14.8, parts can be produced with a maximum density of 98%. For E_0^* below 4.5 no melting took place, whilst>14E_0^*.8 produced excessive melting. The roughness of the surface was shown to vary with beam profile and laser parameters with two activated linear scanning arrays within the laser head generating the lowest surface roughness due to a potential melt-pool re-melting effect. Analyses of microstructure and mechanical properties were conducted. Alpha and beta grains were
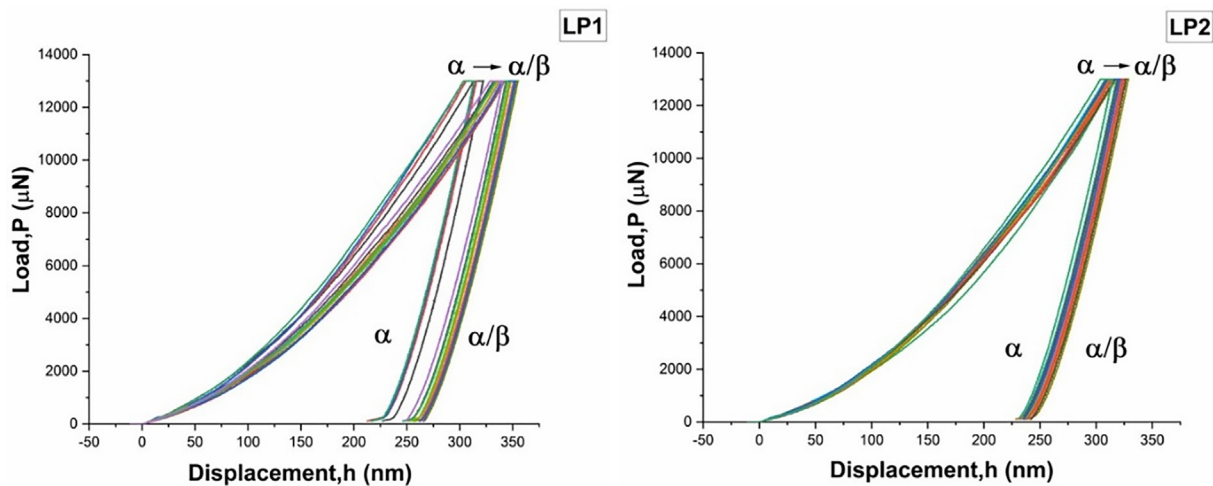
Fig. 21. P-h Curves for samples produced at 75 mm/min for LP1 and LP2.

observed in the XRD analysis in contrast to commercial LPBF systems, which generally produce only alpha grains. The multi-laser DAM process produced much lower cooling rates compared with SLM (600 °C/s compared to 10^7 °C/s), which encouraged the formation of beta grains. A laser beam profile using two linear arrays of lasers generated the slowest cooling rate due to a potential melt pool post-heat/re-melt effect. Samples have been produced with density in excess of 95%, hardness between 4 and 5 GPa and elastic moduli up to 120 GPa. This research demonstrates the potential for using low-power high-efficiency 808 nm diode lasers using this evolved multi-laser fibre coupled DAM approach. The potential to scan large areas simultaneously with enhanced thermal process control has the potential to improve traditional LPBF productivity and efficiency, reduce component thermally induced residual stress, expand list of processable alloy and generate custom microstructures through laser beam profile selection.

Declaration of Competing Interest

The authors declare that they have no known competing financial interests or personal relationships that could have appeared to influence the work reported in this paper.

Acknowledgements

References

[1] D. Herzog, V. Seyda, E. Wycisk, C. Emmelmann, Additive manufacturing of metals, Acta Mater. 117 (2016) 371–392, https://doi.org/10.1016/j.actamat.2016.07.019.

[2] B. Dutta, S. Babu, B. Jared, Comparison of various additive manufacturing technologies, in: B. Dutta, S. Babu, Jared Technology and Applications of Metals in Additive Manufacturing BBT-S (Eds.) Science, Technology and Applications of Metals in Additive Manufacturing. Elsevier, 2019, pp 55–76.

[3] J. Nandy, H. Sarangi, S. Sahoo, A Review on Direct Metal Laser Sintering: Process Features and Microstructure Modeling, Lasers Manuf. Mater. Process. 6 (3) (2019) 280–316.

[4] P. Mishra, T. Ilar, F. Brueckner, A. Kaplan, Energy efficiency contributions and losses during selective laser melting. J. Laser Appl. 30 (2018) 032304. 10.2351/1.5040603.

[5] M. Alsaddah, A. Khan, K. Groom, K. Mumtaz, Use of 450–808 nm diode lasers for efficient energy absorption during powder bed fusion of Ti6Al4V, Int. J. Adv. Manuf. Technol. 113 (9-10) (2021) 2461–2480.

[6] R. Poprawe, C. Hinke, W. Meiners, et al., SLM Production Systems: Recent Developments in Process Development, Machine Concepts and Component Design, 2015, pp 49–65.

[7] M. Brandt, The role of lasers in additive manufacturing, Elsevier Ltd., 2017.

[12] C. Tan, D. Wang, W. Ma, K. Zhou, Ultra-strong bond interface in additively manufactured iron-based multi-materials, Mater. Sci. Eng. A 802 (2021) 140642, https://doi.org/10.1016/j.msea.2020.140642.

[13] C. Tan, K. Zhou, M. Kuang, W. Ma, T. Kuang, Microstructural characterization and properties of selective laser melted maraging steel with different build directions, Sci. Technol. Adv. Mater. 19 (1) (2018) 746–758.

[14] J.H. Martin, B.D. Yahata, J.M. Hundley, J.A. Mayer, T.A. Schaedler, T.M. Pollock, 3D printing of high-strength aluminium alloys, Nature 549 (7672) (2017) 365–369.

[15] X. Zhang, B. Mao, L. Mushongera, et al., Laser powder bed fusion of titanium aluminides: An investigation on site-specific microstructure evolution mechanism, Mater. Des. 201 (2021) 109501, https://doi.org/10.1016/j.matdes.2021.109501.

[16] S. Sanchez, P. Smith, Z. Xu, G. Gaspard, C.J. Hyde, W.W. Wits, I.A. Ashcroft, H. Chen, A.T. Clare, Powder Bed Fusion of nickel-based superalloys: A review, Int. J. Mach. Tools Manuf. 165 (2021) 103729.

[17] K. Kellens, E. Yasa, W. Dewulf, J.R. Duflou, Environmental Assessment of Selective Laser Melting and Selective Laser Sintering, Going Green - Care Innov From Leg Compliance to Energy-efficient Prod. Serv. 4 (2010) 5.

[18] T. Wohlers, Wohlers Report: 3D printing and Additive Manufacturing State of the Industry, ISBN 978-0-9913332-6-4, 2020.

[19] T. Heeling, K. Wegener, The effect of multi-beam strategies on selective laser melting of stainless steel 316L, Addit. Manuf. 22 (2018) 334–342, https://doi.org/10.1016/j.addma.2018.05.026.

[20] R. Kopf, J. Gottwald, A. Jacob, M. Brandt, G. Lanza, Cost-oriented planning of equipment for selective laser melting (SLM) in production lines, CIRP Ann. 67 (1) (2018) 471–474.

[21] H. Lee, C.H.J. Lim, M.J. Low, N. Tham, V.M. Murukeshan, Y.-J. Kim, Lasers in additive manufacturing: A review, Int. J. Precis. Eng. Manuf. Technol. 4 (3) (2017) 307–322.

[22] E. Kennedy, G. Byrne, D.N. Collins, A review of the use of high power diode lasers in surface hardening, J. Mater. Process. Technol. 155156 (2004) 1855–1860, https://doi.org/10.1016/j.jmatprotec.2004.04.276.

[23] M.J. Matthews, G. Guss, D.R. Drachenberg, J.A. Demuth, J.E. Heebner, E.B. Duoss, J.D. Kuntz, C.M. Spadaccini, Diode-based additive manufacturing of metals using an optically-addressable light valve, Opt. Exp. 25 (10) (2017) 11788.

[24] C. Hinke, S. Merkt, F. Eibl, et al., Additive manufacturing: Perspectives for diode lasers, In: Proceedings of the 2015 High Power Diode Lasers and Systems Conference, HPD 2015 - Co-located with Photonex 2015. pp 39–40, 2016.

[25] S. Hengesbach, R. Poprawe, D. Hoffmann, et al., Brightness and average power as driver for advancements in diode lasers and their applications, In: Zediker MS (Ed.) International Society for Optics and Photonics, 2015, p 93480B.

[26] M. Zavala-Arredondo, N. Boone, J. Willmott, D.T.D. Childs, P. Ivanov, K.M. Groom, K. Mumtaz, Laser diode area melting for high speed additive manufacturing of metallic components, Mater. Des. 117 (2017) 305–315.

[27] M. Zavala-Arredondo, H. Ali, K.M. Groom, K. Mumtaz, Investigating the melt pool properties and thermal effects of multi-laser diode area melting, Int. J. Adv. Manuf. Technol. 97 (2018) 1383–1396, https://doi.org/10.1007/s00170-018-2038-2.

[28] M. Zavala, K. Groom, K. Mumtaz, Diode area melting single-layer parametric analysis of 316L stainless steel powder, Int. J. Adv. Manuf. Technol. 1–14 (2017), https://doi.org/10.1007/s00170-017-1040-4.

[29] M. Thomas, G.J. Baxter, I. Todd, Normalised model-based processing diagrams for additive layer manufacture of engineering alloys, Acta Mater. 108 (2016) 26–35, https://doi.org/10.1016/j.actamat.2016.02.025.

[30] A.B. Spierings, M. Schneider, R. Eggenberger, Comparison of density measurement techniques for additive manufactured metallic parts, Rapid Prototyp. J. 17 (2011) 380–386, https://doi.org/10.1108/13552541111156504.

[31] W. Zhang, W. Hou, L. Deike, C.B. Arnold, Using a dual-laser system to create periodic coalescence in laser powder bed fusion, Acta Mater. 201 (2020) 14–22, https://doi.org/10.1016/j.actamat.2020.09.071.

[32] T. Heeling, K. Wegener, Computational Investigation of Synchronized Multibeam Strategies for the Selective Laser Melting Process, Phys. Proc. 83 (2016) 899–908, https://doi.org/10.1016/j.phpro.2016.08.094.

[33] U. Scipioni Bertoli, A.J. Wolfer, M.J. Matthews, J.-P. Delplanque, J.M. Schoenung, On the limitations of Volumetric Energy Density as a design parameter for Selective Laser Melting, Mater. Des. 113 (2017) 331–340.

[34] G.R. Nazami, S. Sahoo, Influence of hatch spacing and laser spot overlapping on heat transfer during laser powder bed fusion of aluminum alloy, J. Laser Appl. 32 (2020) 042007, https://doi.org/10.2351/7.0000157.

[35] I. Yadroitsev, I. Smurov, Surface morphology in selective laser melting of metal powders, Phys. Proc. 12 (2011) 264–270, https://doi.org/10.1016/j.phpro.2011.03.034.

[36] C.Y. Tsai, C.W. Cheng, A.C. Lee, M.C. Tsai, Synchronized multi-spot scanning strategies for the laser powder bed fusion process, Addit. Manuf. 27 (2019) 1–7, https://doi.org/10.1016/j.addma.2019.02.009.

[37] H.Z. Jiang, Z.Y. Li, T. Feng, et al., Factor analysis of selective laser melting process parameters with normalised quantities and Taguchi method. Opt. Laser Technol. 119 (2019) 105592. 10.1016/j.optlastec.2019.105592.

[38] Y.M. Wang, C. Kamath, T. Voisin, Z. Li, A processing diagram for high-density Ti-6Al-4V by selective laser melting, Rapid Prototyp. J. 24 (2018) 1469–1478, https://doi.org/10.1108/RPJ-11-2017-0228.

[39] T. Ahmed, H.J. Rack, Phase transformations during cooling in α+β titanium alloys, Mater. Sci. Eng. A 243 (1998) 206–211, https://doi.org/10.1016/S0921-5093(97)00802-2.

[40] J. Zhang, Y.i. Yang, S. Cao, Z. Cao, D. Kovalchuk, S. Wu, E. Liang, X.i. Zhang, W. Chen, F. Wu, A. Huang, Fine equiaxed β grains and superior tensile property in Ti–6Al–4V alloy deposited by coaxial electron beam wire feeding additive manufacturing, Acta Metall. Sin. (English Lett.) 33 (10) (2020) 1311–1320.

[41] J. Yang, H. Yu, J. Yin, M. Gao, Z. Wang, X. Zeng, Formation and control of martensite in Ti-6Al-4V alloy produced by selective laser melting, Mater. Des. 108 (2016) 308–318.

[42] X. Wang, K. Chou, EBSD study of beam speed effects on Ti-6Al-4V alloy by powder bed electron beam additive manufacturing, J. Alloys Compd. 748 (2018) 236–244, https://doi.org/10.1016/j.jallcom.2018.03.173.

[43] C. Qiu, N.J.E. Adkins, M.M. Attallah, Microstructure and tensile properties of selectively laser-melted and of HIPed laser-melted Ti-6Al-4V, Mater. Sci. Eng. A 578 (2013) 230–239, https://doi.org/10.1016/j.msea.2013.04.099.

[44] L. Thijs, F. Verhaeghe, T. Craeghs, J.V. Humbeeck, J.-P. Kruth, A study of the microstructural evolution during selective laser melting of Ti-6Al-4V, Acta Mater. 58 (9) (2010) 3303–3312.

[45] L. Facchini, E. Magalini, P. Robotti, A. Molinari, Microstructure and mechanical properties of Ti-6Al-4V produced by electron beam melting of pre-alloyed powders, Rapid Prototyp. J. 15 (2009) 171–178, https://doi.org/10.1108/13552540910960262.

[46] J. Cai, F. Li, T. Liu, B. Chen, Investigation of mechanical behavior of quenched Ti-6Al-4V alloy by microindentation, Mater. Charact. 62 (2011) 287–293, https://doi.org/10.1016/j.matchar.2011.01.011.

[47] J. Dong, F. Li, C. Wang, Micromechanical behavior study of α phase with different morphologies of Ti-6Al-4V alloy by microindentation, Mater. Sci. Eng. A 580 (2013) 105–113, https://doi.org/10.1016/j.msea.2013.05.032.

Further reading

[8] D. Buchbinder, H. Schleifenbaum, S. Heidrich, W. Meiners, J. Bültmann, High power Selective Laser Melting (HP SLM) of aluminum parts, Phys. Proc. 12 (2011) 271–278.

[10] J. Metelkova, Y. Kinds, K. Kempen, C. de Formanoir, A. Witvrouw, B. Van Hooreweder, On the influence of laser defocusing in Selective Laser Melting of 316L, Addit. Manuf. 23 (2018) 161–169.

[11] X. Shi, S. Ma, C. Liu, C. Chen, Q. Wu, X. Chen, J. Lu, Performance of high layer thickness in selective laser melting of Ti6Al4V, Materials (Basel) 9 (12) (2016) 975.